

# DYNAMICS OF FE-NI BUBBLES IN YOUNG SUPERNOVA REMNANTS

John M. Blondin, Kazimierz J. Borkowski, and Stephen P. Reynolds

*Department of Physics, North Carolina State University, Raleigh, NC 27695*

## ABSTRACT

Observations of core-collapse supernovae (SNe) have revealed the presence of extensive mixing of radioactive material in SN ejecta. The mixing of radioactive material, mostly freshly synthesized Ni, is not complete, which leads to a two-phase SN ejecta structure. The low-density phase consists of Fe bubbles, created by the energy input from radioactive Co and Ni, surrounded by compressed high-density metal-rich ejecta.

We report on the theoretical investigation of supernova remnant (SNR) dynamics with the two-phase SN ejecta. We first present 3-dimensional hydrodynamic simulations of a single Fe bubble immersed in an outer ejecta envelope, and compare the results with previous work on shock-cloud interactions. We then consider randomly distributed Fe bubbles with an average volume filling fraction of 1/2. We find that the presence of Fe bubbles leads to vigorous turbulence and mixing of Fe with other heavy elements and with the ambient normal-abundance gas. The turbulent energy can be an order of magnitude larger than in the case of smooth ejecta. A significant fraction of the shocked ejecta is found in narrow filaments and clumps moving with radial velocities larger than the velocity of the forward shock. Observational consequences of the two-phase ejecta on SNR X-ray spectra and images are briefly mentioned.

*Subject headings:* hydrodynamics – instabilities – shock waves – ISM: supernova remnants

## 1. INTRODUCTION

The presence of large-scale mixing of ejecta in core-collapse supernovae (SNe) has been well established on both observational and theoretical grounds. The early, unexpected emergence of X-rays and  $\gamma$ -rays shortly after the explosion of SN 1987A provided dramatic evidence for mixing of radioactive Ni throughout the He core and H-rich envelope. Extensive mixing of Ni is also required to explain the light curve and spectral observations of SN 1987A (see McCray 1993 for a review of SN 1987A). From studies of light curves and spectra of numerous core-collapse SNe, it is now known that such large-scale mixing is nearly always present. Another line of evidence is provided by studies of meteoritic graphite grains which condensed in SN ejecta (Travaglio et al. 1999 and references therein). Such grains apparently contained radioactive, short-lived isotopes such as  $^{44}\text{Ti}$  at the time of their formation, which implies extensive mixing of freshly-synthesized material deep in the

SN ejecta with the C-rich layer at the bottom of the He core. This overwhelming observational evidence for mixing is consistent with our present understanding of the collapse and explosion of massive stars. The neutrino-driven Rayleigh-Taylor instability just outside the proto-neutron star leads to convective motions, strengthening the post-bounce shock and maybe even making the explosion possible in many cases (e. g., Mezzacappa et al. 1998; Kifonidis et al. 2000). Further mixing occurs later during the SN explosion because of Rayleigh-Taylor instabilities generated at interfaces between stellar layers with different chemical composition (e.g., Fryxell, Arnett, & Mueller 1991; Hachisu et al. 1992; Kifonidis et al. 2000).

Large-scale turbulence generated during the explosion appears not to be sufficient to mix SN ejecta completely, but only macroscopically. In Cas A, optical observations revealed the presence of ejecta with very different chemical abundances, such as O-, S-, Ar-, and Ca-rich ejecta knots, which were macroscopically mixed during the SN explosion as evidenced by the lack of spatial stratification expected in the absence of mixing (e. g., Fesen & Gundersen 1996). The most recent IR and X-ray observations of Cas A provide further evidence for this macroscopic but not microscopic mixing (Arendt et al. 1999; Douvion et al. 1999; Hughes et al. 2000; Hwang et al. 2000). Spectroscopic observations of numerous SNe also confirm the presence of clumpy ejecta (Spyromilio 1994). Detailed studies of SN 1987A lead to the same conclusion.

In SN 1987A, the inhomogeneities take a particularly interesting form: Fe-Ni bubbles (Li et al. 1993), inferred from observations of Fe, Co, and Ni lines. Ni-rich ejecta clumps, transported outwards by turbulent motions, are heated by their own radioactive energy input, and expand in the ambient substrate of other heavy elements, forming low-density Fe bubbles. The SN structure is then expected to be like a Swiss cheese, with Fe bubbles occupying a substantial ( $\sim 0.5$ ) fraction of the ejecta volume (Li et al. 1993; Basko 1994). These bubbles should lead to vigorous turbulence and mixing in young supernova remnants (SNRs) in general.

Most of ejecta in young SNRs can be seen in X-rays, where modern X-ray observatories such as *Chandra* and *XMM-Newton* have begun to provide high-quality information. Interpretation of these observations must be done in the framework of appropriate hydrodynamical models. But realistic simulations for young SNRs, which include the presence of Fe bubbles in SN ejecta, are lacking. We report here on such 3-dimensional hydrodynamical simulations (preliminary results based on 2-D simulations were reported by Borkowski et al. 2000). Our goal is to study the basic hydrodynamics of the interaction by investigating a single Fe bubble, and to explore how the presence of multiple Fe bubbles changes the global dynamics of young SNRs.

## 2. HYDRODYNAMIC SIMULATIONS

We use a parallel version (implemented with Message Passing Interface) of the Virginia Hydrodynamics (VH-1) numerical code to study the complex dynamics of SNRs with Fe bubbles. The simulations were computed on a spherical grid of  $400^3$  zones covering an angular span of 1.6 stera-

dians. This resolution is comparable to the simulations by Chevalier et al. (1992) that used a grid of  $256^2$ . A higher resolution simulation would show more small scale mixing, but the large-scale dynamics of the problem would not change (Chevalier et al. 1992). Periodic boundary conditions were applied in both the  $\theta$  and  $\phi$  directions. This choice for  $\theta$  is somewhat unorthodox, but we wished to avoid the numerical artifacts associated with the coordinate singularity at  $\theta = 0$ , so we centered our grid about the equator ( $0.3\pi < \theta < 0.7\pi$ ). We experimented with other boundary conditions (e.g., reflecting or zero gradients), but they proved unsatisfactory for various reasons. The numerical grid was expanded to follow the forward blastwave so the evolution could be tracked for many expansion times.

The simulations were initialized with a self-similar driven wave (SSDW) solution (Chevalier 1982) with an ejecta density power law of  $n = 9$  expanding into either a uniform ambient density (an ambient density power law of  $s = 0$ ) or a relic stellar wind (an ambient density power law of  $s = 2$ ). The radial boundary conditions were set to match these power laws. This self-similar structure has the following components: an outer blast wave, a wavy (dynamically unstable) contact discontinuity between the shocked ambient medium and the shocked SN ejecta, and an inner reverse shock. For these parameters, the forward shock decelerates according to  $R_s \propto t^{6/7}$  ( $t^{6/9}$  for  $s = 0$ ), and the reverse shock is located at a radius of  $0.785R_s$  ( $0.842R_s$  for  $s = 0$ ). The initial conditions are spherically symmetric, so the narrow shell of shocked ejecta starts off smooth but eventually shows signs of convective instability (Chevalier et al. 1992).

### 3. DYNAMICS WITH A SINGLE BUBBLE

Hydrodynamical simulations are shown in Figure 1 of a SSDW ( $n = 9$ ,  $s = 2$ ) with a single Fe bubble in the supersonic ejecta. The bubble, with a fractional radius of 0.4 (the radius of the bubble is 0.4 times the distance of the center of the bubble from the center of the SN explosion), is 100 times less dense than the ambient SN ejecta at a radius corresponding to the center of the bubble. The pressure inside the bubble is equal to the pressure of the surrounding ejecta in order to minimize motions, but the Mach number of expansion is still relatively high within the bubble.

The initial contact between the Fe bubble and the reverse shock is illustrated in Figure 1 (left). When the outer edge of the bubble reaches the reverse shock, the reverse shock accelerates into the bubble because of its low density, while a rarefaction wave propagates back into the shocked ejecta. The pressure behind the reverse shock propagating through the bubble drops to more than an order of magnitude smaller than the nominal pressure between the forward and reverse shocks in the spherical SSDW. There is only a modest drop in pressure (compared to the spherical SSDW) in the shocked ambient medium ahead of the bubble because the SNR expansion timescale is comparable to the sound crossing time across the bubble. The high pressure of the relatively tenuous ambient gas then drives dense shocked ejecta deep into the bubble’s interior. This situation is Rayleigh-Taylor unstable, which leads to vigorous mixing of dense shocked ejecta with the low-density shocked Fe from the bubble and the shocked ambient gas. This enhanced mixing is evident

in the middle-left frame of Figure 1. Note that although the reverse shock is moving inwards in this expanding frame, at no time in the simulation is gas ever moving radially inwards in the fixed frame of the explosion.

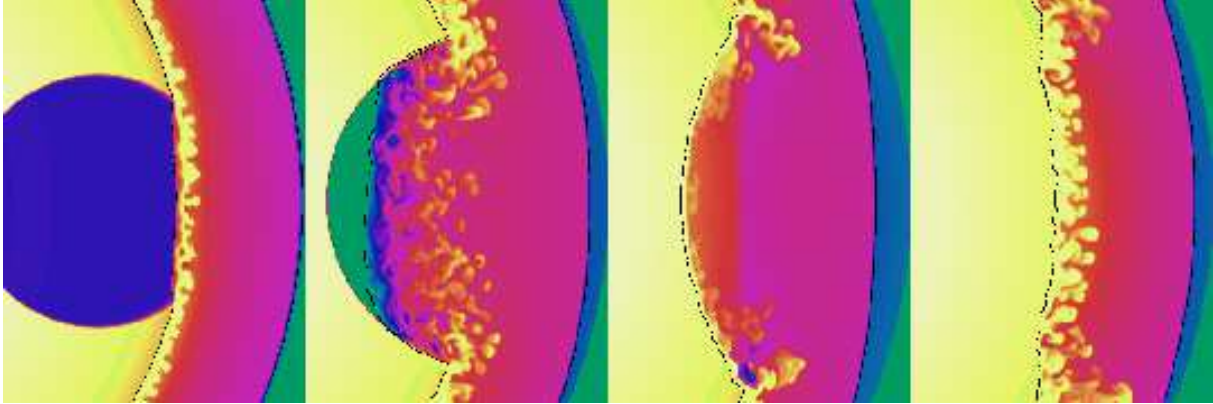


Fig. 1.— Dynamical interaction of an Fe bubble with a SSDW. These 2D slices through the center of the bubble are colored according to gas density, with a logarithmic scale spanning a range of 3.5 orders of magnitude (yellow=high, blue=low). The black lines mark the surface of the forward and reverse shocks. The thin blue strip on the right of each panel marks the undisturbed ambient gas between the forward shock and the edge of the numerical grid. Note the slight deviation of the shock from spherical.

Eventually the reverse shock reflects off the bottom of the bubble (middle-right panel of Figure 1) and propagates back through the layer of mixed gas with a shock Mach number of  $\sim 1.5$ . The reverse shock is also transmitted into the dense ejecta, reforming the thin layer of shocked ejecta present in the initial SSDW. The bottom edge of the bubble is driven back out to the original SSDW by the high density of the ejecta, and in the process the extended layer of mixed gas inside the bubble is swept up and compressed into a thin layer.

The shock reflected from the bubble’s bottom eventually overtakes the blast wave and the layer of shocked ejecta is pushed back to the original radius of the reverse shock. This marks the transition back to the original self-similar stage, and the end of the transient stage associated with the bubble’s presence.

What is less apparent, but perhaps most important, in this simulation is the role of the oblique shocks along the bubble walls in generating vorticity. As the reverse shock traverses the low-density bubble, it drives an oblique shock into the wall of dense ejecta surrounding the bubble. This oblique shock generates vorticity at the bubble’s boundary, and the thin layer of shocked ejecta along the bubble’s wall quickly becomes unstable. This effect is most pronounced along the sides of the bubble where the transmitted shock is very oblique. By the time the bubble has been completely shocked, this excess vorticity has piled up in a thick ring with a radius slightly smaller than the original Fe bubble, as shown in Figure 2. It is this torus of high vorticity where the most vigorous

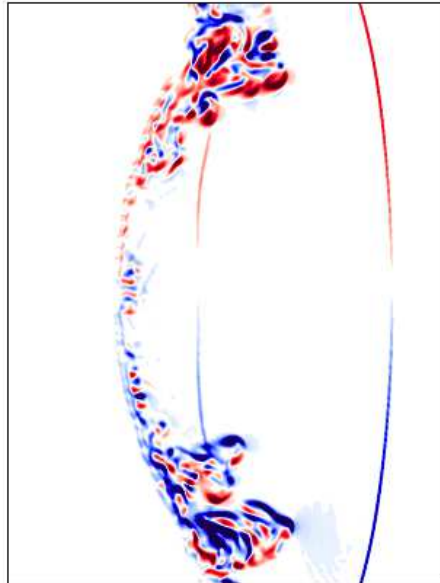


Fig. 2.— A 2D slice through the single bubble simulation, showing the strong vorticity generated in a torus around the side of the bubble. The color corresponds to vorticity (red=positive, blue=negative, white=0). The slightly oblique forward and reflected reverse shocks show up as thin lines of red and blue. This time slice is the same as the middle-right panel in Figure 1.

mixing occurs. This mixing can lead to relatively large velocities, with some shocked ejecta traveling outwards 50% faster than the gas immediately behind the forward shock.

A hydrodynamical problem of a plane shock interacting with a low density spherical (or cylindrical) bubble has been of interest to the fluid dynamics community. Experiments (e. g., Haas & Sturtevant 1987) and hydrodynamical simulations (e. g., Quirk & Karni 1996) revealed how vortex lines (for cylindrical bubbles) and vortex rings (for spherical bubbles) form in this interaction process, although a complete understanding of this complex interaction (including details of mixing of bubble’s material with the ambient medium) is still lacking. Although geometry and dynamics in our simulations are more complex than in these idealized experiments and simulations, the emergence of vortex rings in our simulations is in qualitative agreement with results reported in the literature. We refer the reader to a recent review by Zabusky (1999) for further details about generation of vorticity in shock-accelerated inhomogeneous flows.

This hydrodynamical problem of a shock interacting with a low density bubble can be compared with the more often studied problem of a shock interacting with an overdense cloud (e. g., Klein et al. 1994; Xu & Stone 1995; see also Zabusky 1999 and references therein). In both cases the important long-term result of the shock interaction is the generation of vorticity and a rapid mixing of the gas inside and outside the bubble/cloud. This is demonstrated in a dramatic fashion below when we consider SN ejecta with multiple bubbles instead of a single bubble.

#### 4. DYNAMICS WITH MULTIPLE BUBBLES

A more realistic model of Fe bubbles in SN ejecta should include multiple bubbles occupying a substantial fraction of the ejecta volume. We have evolved such models for both  $s = 0$  (Figure 3) and  $s = 2$  (Figure 4). In these examples, bubbles with a fractional radius of 0.2 and with a uniform density 100 times smaller than the ejecta density are distributed randomly in the ejecta, with an average volume filling fraction of  $\sim 0.5$ . We tracked the filling fraction by computing the fractional area occupied by bubbles at a radius of  $0.5R_s$ . Due to the clustering of bubbles created by the random number generator, the filling fraction went as high as 0.7 and as low as 0.3, but averaged reasonably close to 0.5.

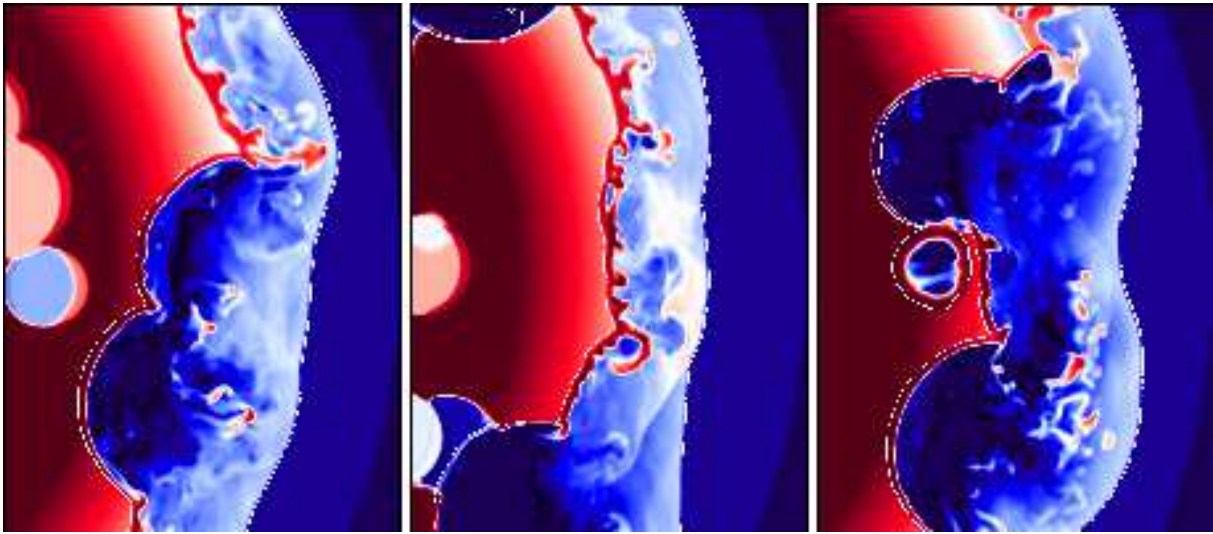


Fig. 3.— Dynamical interaction of multiple Fe bubbles with a SSDW propagating through a uniform ambient medium ( $s = 0$ ). These 2D slices through the center of the simulation show the gas density (red=high, blue=low) along with pressure contours marking the location of the forward and reverse shocks.

The outer shock wave is relatively unaffected by the presence of the Fe bubbles in these simulations; the shape of the outer shock remains relatively spherical and the deceleration parameter ( $Vt/R_s$ ) is within a few percent of the analytic solution of  $6/7$  for a spherical SSDW with  $n = 9$  and  $s = 2$  ( $6/9$  for  $s = 0$ ). The time evolution of the deceleration parameter from both runs is shown in Figure 5. The SSDW has been evolved more than six orders of magnitude in radius, requiring 30,000 timesteps, in order to allow the blastwave to reach a quasi self-similar form (see the time-dependence of turbulent energy density in Figure 9).

In contrast to the forward shock, the presence of multiple bubbles dramatically alters the reverse shock and makes the interaction region very turbulent and inhomogeneous. From the results of the single bubble simulation, we expect the position of the reverse shock to vary randomly on a scale of order the radius of the bubbles. This variation is illustrated in the 2D slices of the multiple

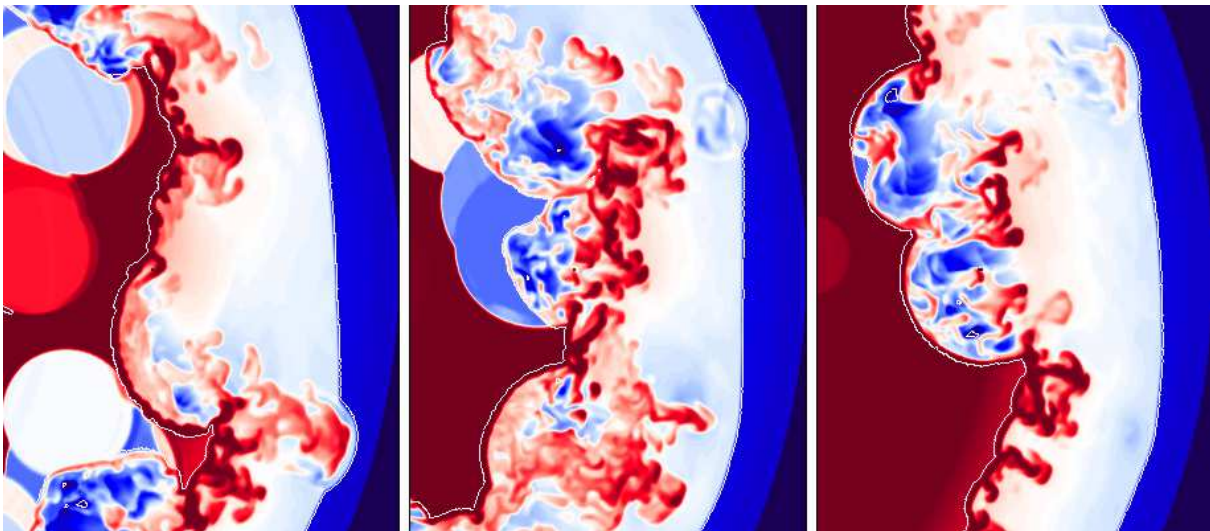


Fig. 4.— Dynamical interaction of multiple Fe bubbles with a SSDW propagating through a relic wind ( $s = 2$ ). These 2D slices through the center of the simulation show the gas density (red=high, blue=low) along with pressure contours marking the location of the forward and reverse shocks. Note the relatively common protrusions through the forward shock driven by clumps of shocked ejecta.

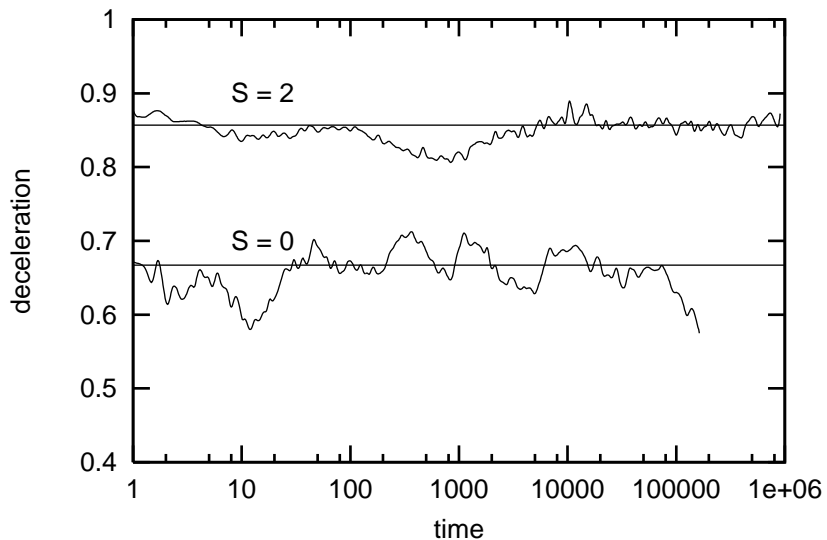


Fig. 5.— Time evolution of the deceleration parameter ( $V_{st}/R_s$ ) for the simulations with multiple bubbles. The straight lines correspond to the analytic values of the deceleration parameter for the corresponding spherically symmetric SSDW.

bubble simulation shown in Figures 3 and 4. The deviations can in fact be much larger than a bubble diameter because of the overlap of bubbles when the filling factor is large. In the  $s = 2$  model the reverse shock came close to the inner radial boundary at  $0.5R_s$  at several times during the simulation. In the  $s = 0$  model we were forced to extend the radial grid beyond  $0.5R_s$  in order to keep the reverse shock contained within the simulation domain. In addition to a strong variation in the radius of the reverse shock, the average radius of the reverse shock is significantly smaller than in the SSDW solution. The average width of the interaction region grows by  $\sim 50\%$  during the first half of the simulations, from the analytic value of 0.21 to an average value of 0.31 for  $s = 2$  and from 0.16 to 0.26 for  $s = 0$ .

Angle-averaged radial profiles of density, turbulent energy, velocity, and pressure for  $s = 0$  (Fig. 6) and  $s = 2$  (Fig. 7) quantitatively demonstrate how the presence of Fe bubbles affects the SNR structure. Density and velocity profiles are remarkably smooth when compared with analytic and numerical solutions for homogeneous ejecta. A spatially-distinct shell of shocked ejecta visible in these solutions is no longer discernible in simulations with bubbles. This nearly complete obliteration of radial structure is not surprising in view of the irregular shape of the reverse shock just discussed. The increase in the width of the interaction region mentioned above is most clearly demonstrated by the broad pressure profiles. Angle-averaged pressures are generally lower than for homogeneous ejecta because of the presence of unshocked ejecta with negligible pressure throughout the interaction region. In the vicinity of the blast wave angle-averaged pressure is also lower because of the presence of the unshocked ambient gas located between the blast wave protrusions.

The irregular shape of the reverse shock has an important effect on the dynamics of the SNR. If a region of interbubble ejecta encounters a relatively oblique reverse shock, it will be decelerated less than it would in a spherically symmetric SSDW. This dense region would then propagate through the intershock region to produce a protrusion of the forward shock. In effect, the geometry of the interbubble ejecta produced small overdense regions that behaved more like clumps within low-density ejecta than bubbles within high-density ejecta. The regions of interbubble ejecta that appeared to have the most effect on the intershock region were comparable in size to the bubbles themselves. Larger regions of ejecta without bubbles resulted in a relatively planar reverse shock, while smaller regions of ejecta between bubbles did not significantly perturb the intershock region.

However, even in the most favorable scenario, regions of dense shocked ejecta traveling through the intershock region were quickly disrupted by fluid instabilities and ultimately had a minimal impact on the forward shock. Dense clumps being slowed by the more tenuous shocked ambient gas are Rayleigh-Taylor unstable, while shear flow around the clumps creates Kelvin-Helmholtz instability. Both processes act to spread out the clump laterally and increase the drag. The result is that any dense clump creating a protrusion of the forward shock is almost immediately sheared apart, with the remaining pieces quickly advected back into the intershock region. Note that these same processes are responsible for shaping the shell of shocked ejecta in the case of spherically-symmetric ejecta (Chevalier et al. 1992). In the absence of Fe bubbles, however, the drag within



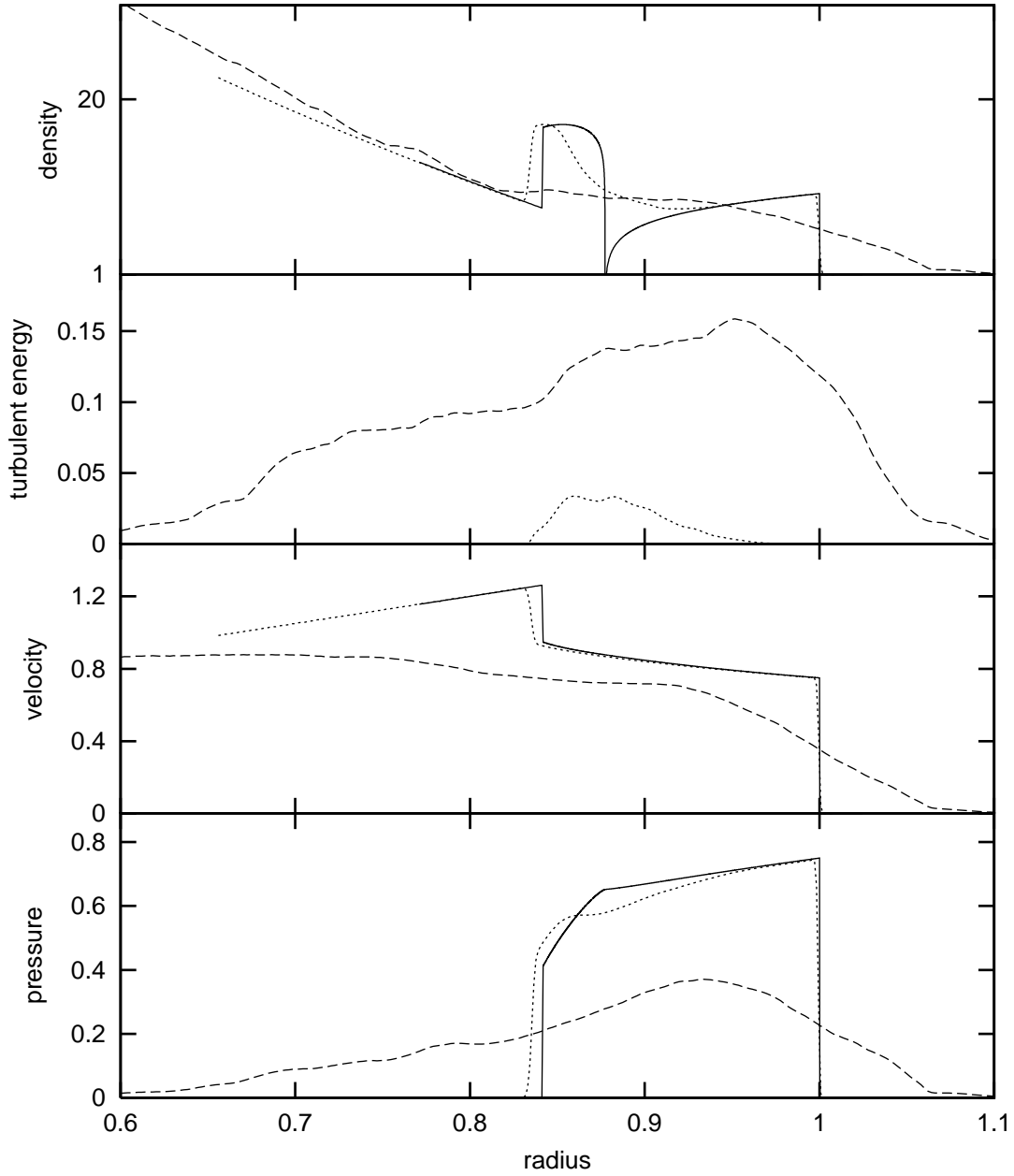


Fig. 6.— Angle-averaged radial profiles for  $s = 0$ , comparing the 3D Fe-Ni bubble simulation (solid lines), a 3D simulation with smooth ejecta (dashed lines), and the analytic 1D solution (dotted lines). The density is scaled to the preshock density,  $\rho_0$ , the velocity is scaled to the shock velocity,  $V_s$ , and the pressure and turbulent kinetic energy density are scaled to  $\rho_0 V_s^2$ .

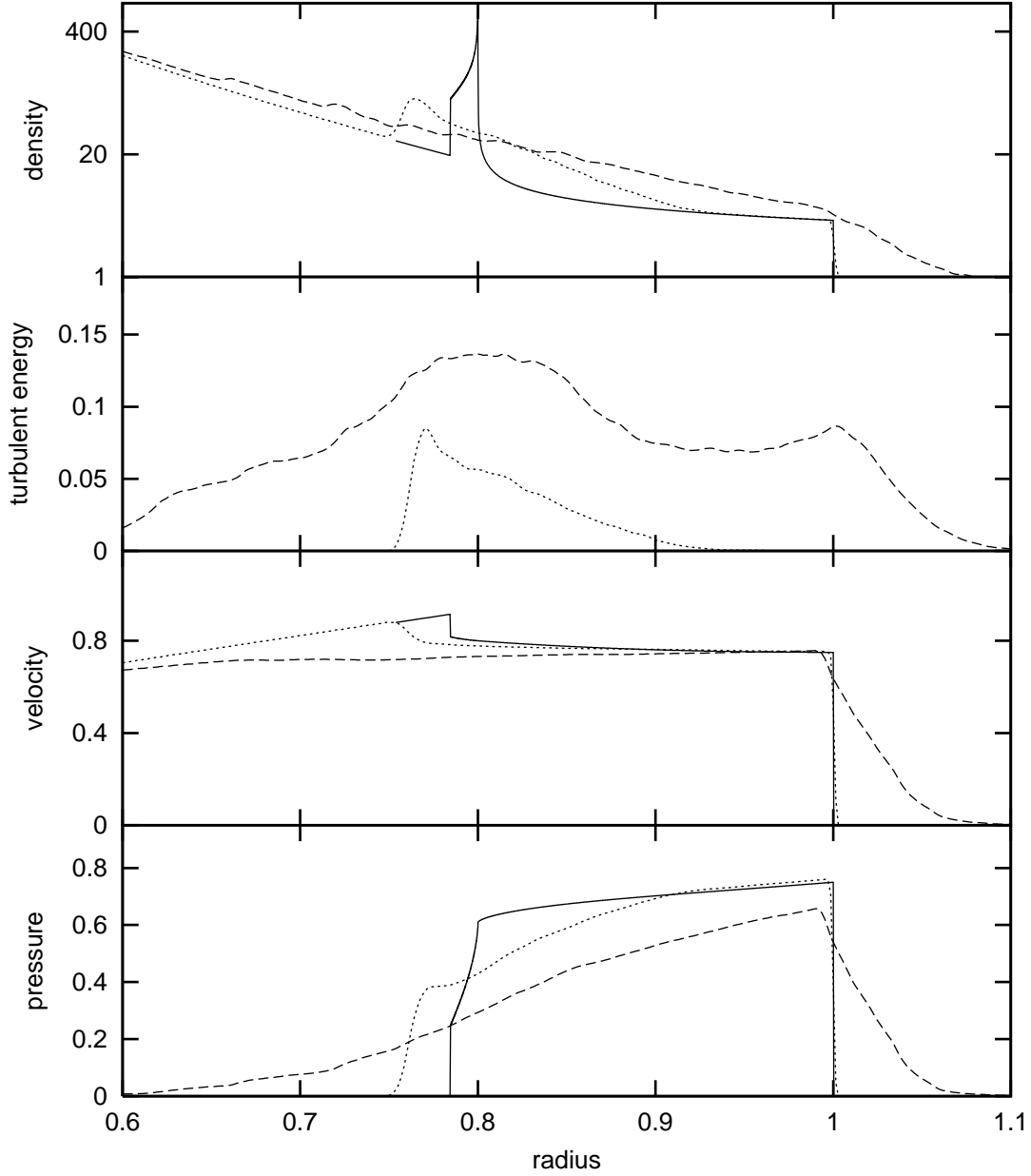


Fig. 7.— Angle-averaged radial profiles for  $s = 2$ , comparing the 3D Fe-Ni bubble simulation (solid lines), a 3D simulation with smooth ejecta (dashed lines), and the analytic 1D solution (dotted lines). The density is scaled to the preshock density,  $\rho_0$ , the velocity is scaled to the shock velocity,  $V_s$ , and the pressure and turbulent kinetic energy density are scaled to  $\rho_0 V_s^2$ .

the intershock region prevented the shocked ejecta from getting anywhere close to the shock front.

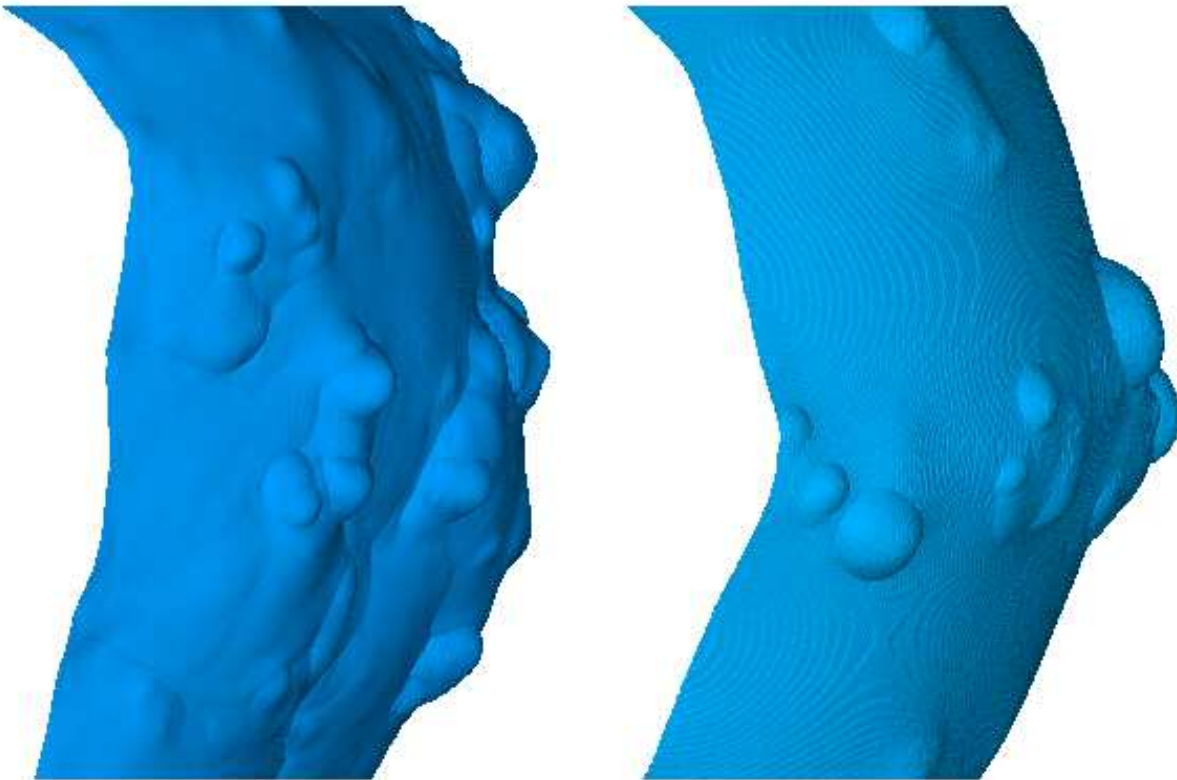


Fig. 8.— Deformations of the forward shock due to Fe bubbles in the SN ejecta, for  $s = 0$  (left) and  $s = 2$  (right).

The impact of these ejecta clumps on the shape of the forward shock is shown in Figure 8. The most pronounced deformations of the forward shock were relatively small wavelength (less than a bubble radius) protrusions driven by clumps of shocked ejecta. Some of these protrusions pushed the forward shock out an extra 15%, while longer wavelength variations in the radius of the forward shock were limited to only a few percent. Angle-averaged profiles (Figs. 6 and 7) show that  $\leq 5\%$  excursions of the blast wave are common.

Wang & Chevalier (2000) arrived at similar conclusions regarding clumpy ejecta, namely that even extremely overdense clouds have relatively little effect on the forward shock. They used 2D simulations to study the evolution of a small, dense cloud placed in the ejecta of a Type Ia SN model in which the nominal ejecta are described by an exponential density profile. As long as sufficient spatial resolution was provided, their overdense clumps were flattened out and broken up by fluid instabilities before they reached the shock front. In 3D and with higher numerical resolution, this process should happen even faster.

The dynamics in these multiple-bubble simulations appear much richer than isolated bubbles

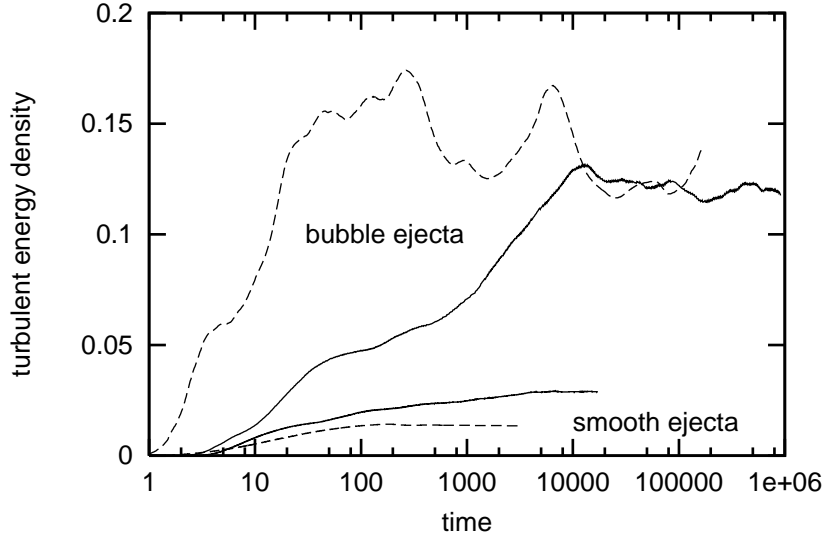


Fig. 9.— Time evolution of the turbulent energy density within the intershock region, for the simulations with multiple bubbles. Dashed lines:  $s = 0$ . Solid lines:  $s = 2$ .

or clouds alone. In the multiple bubble simulations the propagation of the reverse shock through bubbles and around interbubble regions leads to a substantial amount of turbulence in the intershock region. We tracked the turbulent energy density in the intershock region by summing up the transverse (non-radial) kinetic energy in each zone between the reverse and forward shocks. We adjusted this value by  $3/2$  to account for the radial component of the turbulent flow (i.e., we assume all three components of the turbulent flow have comparable magnitude:  $v_r^2 \sim v_\theta^2 \sim v_\phi^2$ ). This average was then normalized by the kinetic energy density flowing through the shock front,  $\rho_o V_s^2$ . The results are plotted as a function of radius in Figures 6 and 7, and as a function of time in Figure 9. In contrast to the case of homogeneous ejecta, the turbulent region is no longer restricted to the shocked ejecta and the adjacent shocked ambient gas. The turbulence extends across the whole interaction region, as implied by broad, slowly varying turbulent energy profiles. The average turbulent energy density grows relatively slowly, but eventually reaches a significant fraction ( $> 10\%$ ) of the energy density associated with the forward shock.

## 5. OBSERVATIONAL CONSEQUENCES

### 5.1. Gas Temperature and Velocity

The irregular shape of the reverse shock has important implications regarding the X-ray spectrum produced by these SNR models. Any deviation from a spherical shock will decrease the shock velocity and hence the postshock temperature. From Figures 3 and 4 we see that this will be mildly

important for the forward shock, but can be expected to have dramatic effects for the reverse shock. Furthermore, as the reverse shock moves backward through a bubble (in the expanding frame), the shock velocity can be higher than in the spherical case, resulting in higher postshock temperatures (but with small emission measure because of the low density).

To estimate these effects without undertaking the complicated effort of calculating X-ray spectra, we have summed up the emission measure (EM) for each zone in the simulation, and plotted this as a function of temperature and radial velocity (scaled to the postshock temperature and shock velocity). (This is only a very approximate procedure as we neglected variations in the mean molecular weight between Fe bubbles and the ambient ejecta. For detailed comparisons with X-ray observations one also needs to consider electron temperature which is generally lower than the mean gas temperature discussed here.)

The results for both the  $s = 2$  and  $s = 0$  multiple bubble simulations are shown in Figures 10 and 11. Superimposed on these plots are the curves corresponding to emission from spherically symmetric SSDWs. In both cases these curves are composed of two pieces, one for the shocked ejecta and one for the shocked ambient gas. Shocked gas immediately behind the forward shock is located at  $\log(T) = 0$  and  $V = 0.75$ . For the  $s = 2$  case the gas temperature in the SSDW decreases with increasing distance from the forward shock, while the opposite holds for  $s = 0$ . Shocked ejecta immediately behind the reverse shock are located at  $\log(T) = -1.76$  and  $V = 0.82$  and decrease in temperature away from the shock in the case of  $s = 2$ . For  $s = 0$ , the shocked ejecta start off at  $\log(T) = -0.75$  and  $V = 0.95$  and increase in temperature away from the shock. Despite these differences in the spherically symmetric models, the emission maps from the 3D simulations with multiple bubbles appear relatively similar. In both cases X-ray emitting gas is significantly spread out in temperature. This is most dramatic in the  $s = 0$  case, for which there is no cool gas in the spherical solution.

There is also a large spread in the radial velocity of the X-ray emitting gas, particularly for the case of  $s = 0$ . In both simulations the radial velocity of the shocked ambient gas is spread to lower velocities as a result of protrusions in the forward shock, while the radial velocity of the shocked ejecta is spread to higher velocities. In the case of  $s = 0$ , the bulk of the X-ray emitting ejecta is traveling faster than the forward shock.

## 5.2. SNR Morphology

To provide a qualitative estimate of how Fe bubbles might affect the observed morphology of SNRs, we created a volume rendering of the emission measure of shocked gas computed from the last frame in our multiple-bubble simulations. While the actual emission observed from a SNR will also depend on the local temperature, abundance, and ionization, the emission measure provides a simple, convenient means for exploring the X-ray morphology implied by a given hydrodynamical model. As such, these images are meant only to show an overall qualitative agreement with the

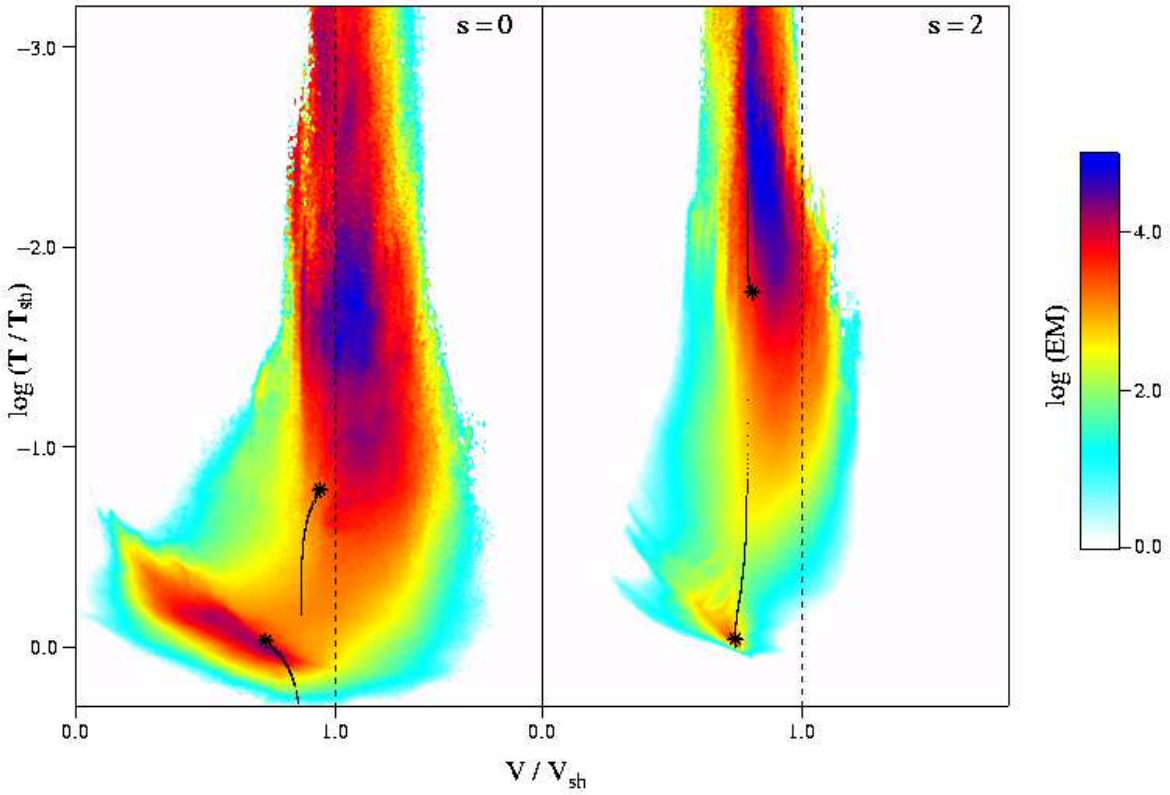


Fig. 10.— A map of the emission measure as a function of temperature and radial velocity for both the  $s = 0$  and  $s = 2$  simulations. The temperature is scaled to the postshock temperature, and the velocity is scaled to the velocity of the forward shock. The black lines map out the region of emission for the corresponding spherical SSDW, with stars at their ends marking shock locations. Note that while the analytic solutions differ considerably between  $s = 0$  and  $s = 2$ , the results of the 3D hydrodynamic simulations with Fe bubbles are quite similar.

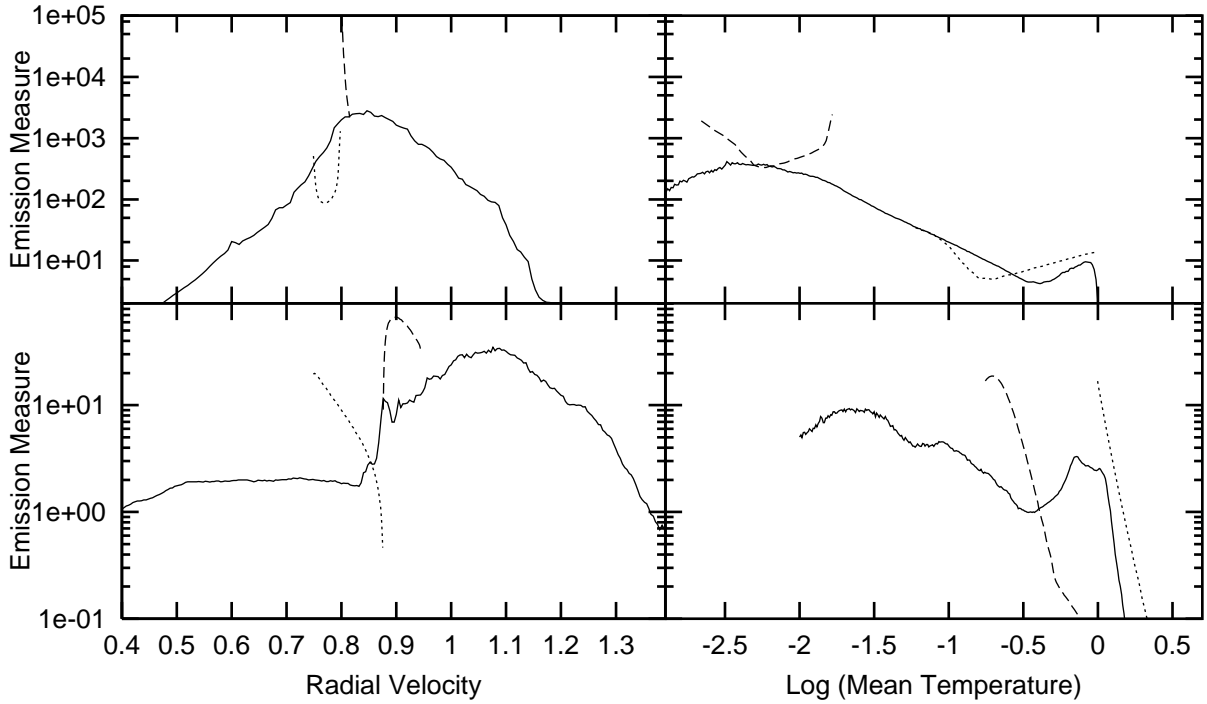


Fig. 11.— The emission measure as a function of temperature and radial velocity for both the  $s = 0$  (bottom) and  $s = 2$  (top) simulations. The temperature is scaled to the postshock temperature, and the velocity is scaled to the velocity of the forward shock. The solid lines correspond to the 3D simulation with Fe-Ni bubbles. For comparison, we also plot the emission measure from the shocked ejecta (dashed lines) and shocked ambient medium (dotted lines) in the corresponding 1D self-similar solutions.

observed X-ray morphology of SNRs like Cas A.

The rendered images shown in Figure 12 are dominated by narrow filaments of shocked ejecta. These filaments are barely resolved in our numerical simulations, and they occupy a very small fraction of the volume of the SNR. In the  $s = 2$  model, 90% of the EM comes from less than 2% of the volume of shocked gas. These filaments often show up as rings or partial rings representing the circumference of Fe bubbles as they pass through the reverse shock. These rings show up more prominently in the  $s = 0$  simulation.

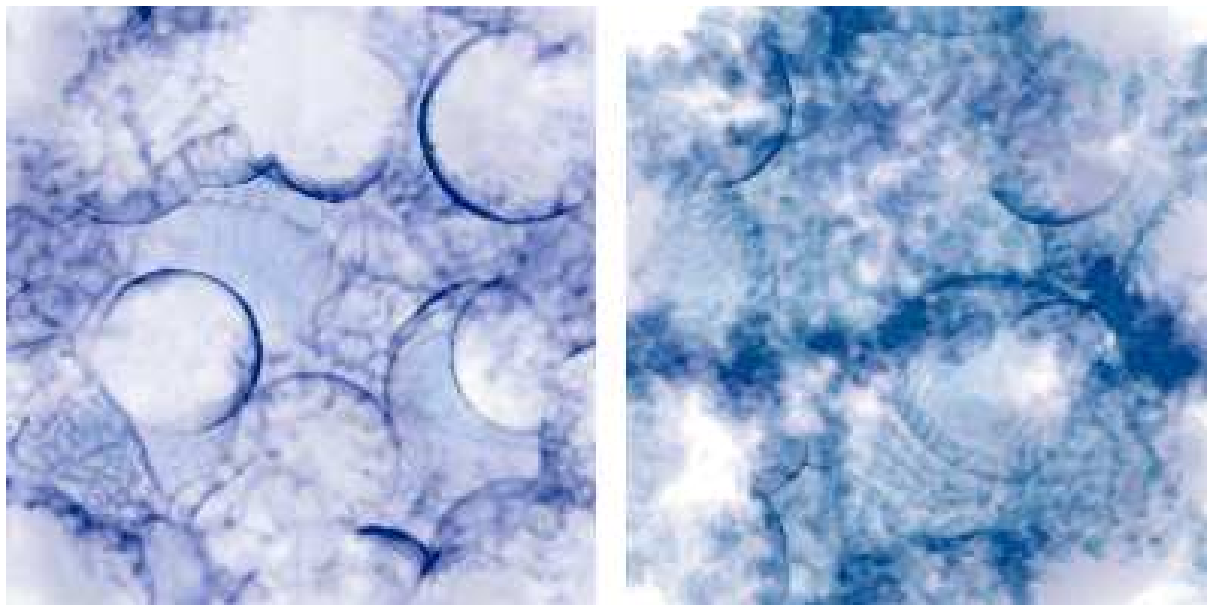


Fig. 12.— A volume rendering of the gas density from the multiple bubble simulations ( $s = 0$  on the left,  $s = 2$  on the right), illustrating the prominence of the filaments of shocked ejecta. This view is looking down onto the simulation such that the SSDW is propagating up out of the page.

## 6. SUMMARY

Our primary conclusion is that large-scale inhomogeneities associated with the presence of Fe bubbles in heavy-element ejecta lead to vigorous turbulence and mixing in young SNRs. The turbulent energy density may be increased by an order of magnitude when compared with homogeneous ejecta. This turbulence radically changes the spatial structure of the interaction region between the blast wave and the reverse shock. While the time-averaged dynamics and the propagation of the forward shock are well described by a self-similar solution (Chevalier 1982; Chevalier et al. 1992), the reverse shock geometry and the structure of the shocked region are very different in the presence of the Fe bubbles. The reverse shock is no longer approximately spherically symmetric, and jet-like fingers of ejecta can even affect the location of the blast wave. Angle-averaged density profiles



rise smoothly toward the remnant’s interior, with no signs for the presence of a spatially distinct shell of ejecta. Pressure and temperature variations of orders of magnitude are also present, unlike the case of homogeneous ejecta which can be described by well-defined density, pressure, and temperature profiles. Such large variations should dramatically influence X-ray emission, which depends strongly on temperature and density. In particular, low temperature, dense ejecta are particularly efficient in producing X-ray emission, and may dominate X-ray spectra. But this emission is generally produced by ejecta which suffered the least amount of deceleration, so that their radial velocities and proper motions may be even higher than that of the blast wave. This example demonstrates that standard SSDW solutions should be used with an extreme caution for young SNRs with inhomogeneous ejecta. The amount of turbulence generated by the presence of Fe bubbles in SNRs most likely varies from remnant to remnant because of large ( $\sim 100$ ) variations in the radioactive Ni yields in core-collapse SNe. In addition, the amount of turbulence might be lower for those SNRs which did not have enough time to enter the self-similar turbulent regime, because of long timescales necessary to achieve it. But unless mixing of heavy elements is somehow inhibited during a SN explosion, it should be clear that one-dimensional models are clearly not acceptable for remnants of core-collapse SNe, and that multidimensional hydrodynamical modeling is essential for understanding dynamics of heavy-element ejecta in such remnants. It is also possible that Ni bubbles can be formed in Type Ia supernova explosions (Wang & Chevalier 2000), so that our results may be applicable there as well.

We expect that small-scale turbulence will have a strong effect on the synchrotron radio morphology of a young remnant. In 2-D MHD simulations of the SSDW phase of a young Type Ia ( $s = 0$ ) supernova remnant, Jun & Norman (1996) found that turbulent energy eventually rose to about 0.6% of the kinetic energy in the remnant, and that random magnetic energy rose as well, to a level of about 0.3% of the turbulent energy. The random magnetic-field energy did not track the total turbulent energy precisely, but spatial locations of strong turbulence (Kelvin-Helmholtz unstable edges of Rayleigh-Taylor fingers) were also the locations of strong magnetic-field amplification. In synchrotron visualizations, Jun & Norman (1996) also found that regions of strong magnetic field produced strong synchrotron emission, but their simulation used a relatively simple description of relativistic-electron acceleration and transport. We expect that magnetic fields in a bubble simulation would also track locations of turbulence and vorticity, that is, should indicate bubble walls, and ought to be noticeable in synchrotron images. In addition, the far higher levels of turbulent energy we find compared to smooth ejecta models such as Jun and Norman’s should result in considerably higher magnetic energy densities and consequent higher synchrotron emissivities. However, hydrodynamic simulations including magnetic-field tracking and particle acceleration and subsequent evolution will be necessary to make more definite predictions.

Our results are in qualitative agreement with the observed morphology of Cas A, undoubtedly the best example of a young SNR with ample evidence for vigorous mixing. Our simulations are able to reproduce filamentary ejecta emission seen in *Chandra* images. The ragged appearance of Cas A, including its “jet” feature, may also be a consequence of an interaction of bubbly ejecta with

the ambient medium, and not necessarily the result of a strongly asymmetric explosion. It is also tempting to identify its rings of optical knots (Reed et al. 1995) with the most dense ejecta clumps at the boundaries of Fe bubbles. Our current simulations are however not suitable for a detailed modeling of the Cas A dynamics because of the evidence for the dynamically important shell of circumstellar matter in Cas A (Chevalier & Liang 1989). The circumstellar interaction, studied by us through one-dimensional hydrodynamical simulations (Borkowski et al. 1996), must be now simulated in 3-D in the framework of bubbly ejecta. A quantitative study of spatial morphology of Cas A, coupled with a more detailed examination of spatial structures in hydrodynamical data sets, would also be useful.

X-ray observations should provide a most complete test of the two-phase model, because they probe the bulk of the shocked material. While modeling of X-ray emission based on multidimensional calculations clearly demands a separate effort, we briefly outline what major effects are expected. If most Fe initially resides in low-density shocked bubbles, while other heavy elements are located in the dense phase of SN ejecta, then Fe lines should generally be much weaker than lines from other abundant heavy elements. Fe lines indeed appear to be weaker than expected in Cas A (Borkowski et al. 1996; Vink et al. 1996; Favata et al. 1997) when compared with strong Si, S, Ar, and Ca lines, based on nucleosynthetic yields of core-collapse SNe. Unlike in the optical and IR, freshly synthesized Fe was detected by *Chandra* (Hughes et al. 2000; Hwang et al. 2000), but its spatial distribution is different than that of Si- and S-rich ejecta. This means that not all Fe resided in low-density bubbles, either because of microscopic mixing of Fe at the bubbles' boundaries or because radioactive Ni was mixed to sufficiently high velocities where the bubble growth was inhibited by escape of  $\gamma$ -rays from Ni clumps. Quantitative analysis of *Chandra* Cas A data, coupled with hydrodynamical simulations and X-ray modeling, should provide a stringent test of the two-phase ejecta model with Fe bubbles.

As remnants become older, turbulent mixing will lead to a gradual strengthening of Fe lines with respect to other heavy elements. Even if Fe is microscopically mixed with other elements during the SNR evolution, its ionization age should lag behind that of other elements. In the next few years, a combination of new X-ray observations and sophisticated hydrodynamical and X-ray modeling should provide us with a vastly better understanding of how chemical elements are ejected in explosions of massive stars and how they are dispersed into ambient interstellar medium.

We thank Dick McCray for discussions about Fe-Ni bubbles in SN 1987A. The three-dimensional simulations reported here were performed at the North Carolina Supercomputing Center using 100 processors of an IBM SP2. We thank NCSC and IBM for their generous support of computing resources. Support for this work was provided by NASA under grant NAG-7153.

## REFERENCES

Arendt, R. G., Dwek, E., & Moseley, S. H. 1999, *ApJ*, 521, 234

- Basko, M. 1994, *ApJ*, 425, 264
- Borkowski, K. J., Blondin, J. M., Lyerly, W. J., & Reynolds, S. P. 2000, in *AIP Conference Proceedings* 522, “Cosmic Explosions”, eds. S. S. Holt & W. W. Zhang, 173
- Borkowski, K. J., Szymkowiak, A. E., Blondin, J. M., & Sarazin, C. L. 1996, *ApJ*, 466, 866
- Chevalier, R. A. 1982, *ApJ*, 258, 790
- Chevalier, R. A., Blondin, J. M., & Emmering, R. T. 1992, *ApJ*, 392, 118
- Chevalier, R. A., & Liang, E. P. 1989, *ApJ*, 344, 332
- Douvion, T., Lagage, P. O., & Cesarsky, C. J., 1999, *A&A*, 352, L111
- Favata, F., et al. 1997, *A&A*, 324, L49
- Fesen, R. A., & Gunderson, K. S. 1996, *ApJ*, 470, 967
- Fryxell, E., Arnett, D., & Mueller, E. 1991, *ApJ*, 367, 619
- Haas, J., & Sturtevant, B. 1987, *J. Fluid Mech.*, 181, 41
- Hachisu, I., Matsuda, T., Nomoto, K., & Shigeyama, T. 1992, *ApJ*, 390, 230
- Hughes, J. P., Rakowski, C. E., Burrows, D. N., & Slane, P. O. 2000, *ApJ*, 528, L109
- Hwang, U., Holt, S. S., & Petre, R. 2000, *ApJ*, 537, L119
- Jun, B.-I., & Norman, M. L. 1996, *ApJ*, 465, 800
- Kifonidis, K., Plewa, T., Janka, H.-Th., & Müller, E., 2000, *ApJ*, 531, L523
- Klein, R. I., McKee, C. F., & Colella, P. 1994, *ApJ*, 420, 213
- Li, H., McCray, R., & Sunyaev, R. A. 1993, *ApJ*, 419, 824
- McCray, R. 1993, *ARAA*, 31, 175
- Mezzacappa, A., Calder, A. C., Bruenn, S. W., Blondin, J. M., Guidry, M. W., & Umar, A. S. 1998, *ApJ*, 495, 911
- Quirk, J. J., & Karni, S. 1996, *J. Fluid Mech.*, 318, 129
- Reed, J. E., Hester, J. J., Fabian, A. C., & Winkler, P. F. 1995, *ApJ*, 440, 706
- Spyromilio, J. 1994, *MNRAS*, 266, L61
- Travaglio, C., Gallino, R., Amari, S., Zinner, E., Woosley, S., & Lewis, R. S. 1999, 510, 325

Vink, J., Kaastra, J. S., & Bleeker, J. A. M. 1996, *A&A*, 307, L41

Wang, C.-Y. & Chevalier, R. A. 2000, *ApJ*, submitted

Xu, J., & Stone, J. M. 1995, *ApJ*, 454, 172

Zabusky, N. J. 1999, *Ann. Rev. Fluid Mech.*, 31, 495